Eur. Phys. J. Plus (2020) 135:647
https://doi.org/10.1140/epjp/s13360-020-00635-x

THE EUROPEAN PHYSICAL JOURNAL PLUS

Regular Article

Comparison of the performance of two handheld XRF instruments in the study of Roman tesserae from Cástulo (Linares, Spain)

Mafalda Costa[1,2,a], **Anastasia Rousaki**[3,b], **Sylvia Lycke**[2,3,c], **Delphine Saelens**[2,d], **Pieter Tack**[4,e], **Alberto Sánchez**[5,f], **José Tuñón**[5,g], **Bautista Ceprián**[5,h], **Pilar Amate**[5,i], **Manuel Montejo**[6,j], **José Mirão**[1,7,k], **Peter Vandenabeele**[2,3,l]

[1] HERCULES Laboratory, University of Évora, Palácio do Vimioso, Largo Marquês de Marialva 8, 7000-809 Évora, Portugal
[2] Archaeometry Research Group, Department of Archaeology, Ghent University, Sint- Pietersnieuwstraat 35, 9000 Ghent, Belgium
[3] Raman Spectroscopy Research Group, Department of Chemistry, Ghent University, Krijgslaan 281, S12, 9000 Ghent, Belgium
[4] X-ray Micro-spectroscopy and Imaging Research Group, Department of Chemistry, Ghent University, Krijgslaan 281, S12, 9000 Ghent, Belgium
[5] University Research Institute for Iberian Archaeology, University of Jaén, Building C6, 23071 Jaén, Spain
[6] Department of Physical and Analytical Chemistry, University of Jaén, Building B2, 23071 Jaén, Spain
[7] Department of Geosciences, School of Science and Technology, University of Évora, Colégio Luís António Verney, R. Romão Ramalho, 59, 7000-671 Évora, Portugal

Received: 28 May 2020 / Accepted: 27 July 2020 / Published online: 11 August 2020

Abstract Cultural Heritage objects are frequently unavailable for transportation to laboratory facilities due to their size, location or local Cultural Heritage preservation regulations. The development of handheld XRF (hXRF) systems has, therefore, proven to be essential in the study of unmovable objects. In this study, two handheld XRF instruments—Bruker™ Tracer III SD® and Olympus™ Innov-X Delta Premium—were compared and evaluated

Electronic supplementary material The online version of this article (https://doi.org/10.1140/epjp/s13360-020-00635-x) contains supplementary material, which is available to authorized users.

[a] e-mail: mcosta@uevora.pt
[b] e-mail: anastasia.rousaki@ugent.be
[c] e-mail: sylvia.lycke@ugent.be
[d] e-mail: delphinesaelens@gmail.com
[e] e-mail: pieter.tack@ugent.be
[f] e-mail: vizcaino@ujaen.es
[g] e-mail: jtunon@ujaen.es
[h] e-mail: bceprian@ujaen.es
[i] e-mail: mamate@ujaen.es
[j] e-mail: mmontejo@ujaen.es
[k] e-mail: jmirao@uevora.pt
[l] emails: peter.vandenabeele@ugent.be; raman@ugent.be (corresponding author)

using tesserae from the *Mosaico de los Amores* (Linares, Spain). Given their portability, the user-friendly nature of their operating systems and their overall performance, both hXRF instruments are highly recommended for in situ campaigns in Cultural Heritage studies. However, the detection limits calculated for each element point towards a better detection of low-Z elements when using the two-beam mode of the Olympus™ Innov-X Delta Premium hXRF. This study underlines the importance of systems that allow the analysis of the same point with analytical conditions optimized for different chemical elements.

1 Introduction

X-ray fluorescence (XRF) has been used in archaeometry since the 1960s [1]. The need for portable and handheld XRF (hXRF) devices, while not exclusive to the art and archaeology market, is essential in the study of unmovable objects. The miniaturization of X-ray tubes and Peltier-cooled detectors, as well as the introduction of X-ray beam controllers (e.g. collimators), enabled the development of portable and handheld XRF systems in the late twentieth and early twenty-first centuries [2–4]. The introduction of silicon drift detectors (SDD) in hXRF instruments in 2008 increased energy resolution, lowered the detection limits and allowed the determination of light elements such as Mg, Al and Si [5].

Cultural Heritage objects are frequently unavailable for transportation to laboratory facilities due to their size, location or local Cultural Heritage preservation regulations. The development of user-friendly software that requires little or no previous experience with XRF analysis, as well as the size, shape and weight of most commercial hXRF systems, makes this non-invasive technique well suited for in situ measurements in non-laboratory settings such as museums and archaeological excavations. The "point and shoot" feature of hXRF, when combined with the low cost of the devices, can explain the growing use of this technique in the study of ceramics, glass and stone, among others (e.g. [6–16]). However, it is important to point out that XRF has limited use in the analysis of multi-layered artefacts [17]. The existence of corrosion or weathering layers, for instance, can greatly influence the results obtained [17, 18]. Surface roughness can also introduce additional errors, and infinite thickness, calculated based on X-ray penetration depth, is required [17, 18].

Moreover, difficulties can arise during the interpretation of XRF results due to spectral interferences, artefact peaks and matrix effects. Bremsstrahlung caused by the deceleration of electrons as they strike the anode of the X-ray tube and the products of elastic scattering (Rayleigh scattering) and inelastic scattering (Compton scattering) are usually present in an XRF spectrum [19]. However, while high energy resolution is important to mitigate spectral interferences or overlap effects, the use of deconvolution software is also essential.

The interaction between the X-ray fluorescence photons from the sample and the detector can also lead to the formation of artefact peaks. Sum peaks occur when two photons arrive at the detector within a sufficiently short time frame, while escape peaks occur when a portion of the energy of the incoming photons is reemitted by the atoms of the detector and cast away from the detector material. Matrix effects are caused by fluorescent radiation that is absorbed by coexisting elements leading to either a decreased intensity of the characteristic X-rays of the element or to an increased intensity when an enhancement of fluorescent radiation occurs due to secondary radiation from the element itself or coexisting elements. Fortunately, most spectral interferences are, nowadays, successfully eliminated by corrections introduced in spectral evaluation software [19].

When quantitative analysis is required, developing calibrations targeted to the material under analysis is essential to optimize data quality, as pre-set factory calibration methods

generally deliver sub-optimal results [20]. The use of certified reference materials (CRMs) is essential to determine the instrument's accuracy and precision. Empirical calibration and fundamental parameters (FP) calibration are the two most commonly used calibration approaches in XRF analysis. In order to produce a reliable empirical calibration model, the CRMs chosen must have similar matrices and elemental concentrations as the samples under analysis [21, 22]. In this case, a combination of the use of appropriate CRMs and regression mathematics accounts for elemental response and matrix effects [21]. In FP methods, on the other hand, interelement coefficients are predetermined, while background and overlap corrected net intensities are converted into elemental concentrations [21].

Several authors have concluded that hXRF and benchtop XRF instruments yield comparable elemental characterization results [22–24]. However, only a limited number of studies compare handheld instruments in archaeometric contexts [25]. In this study, two handheld XRF instruments—Bruker™ Tracer III SD® and Olympus™ Innov-X Delta Premium—were compared and evaluated using tesserae from the *Mosaico de los Amores* (Linares, Spain).

2 Materials and methods

2.1 Mosaico de los Amores

The Iberian-Roman city of Cástulo, located on the right bank of the Guadalimar river (Upper Guadalquivir valley) and ca. 5 km south of the city of Linares, was occupied since the 3rd millennium B.C. until the fifteenth century A.D. Built in the form of an *oppidum*, with the characteristic fortified walls, Cástulo was surrounded by up to eight necropolises [26]. Its strategic location in the vicinity of the Sierra Morena mountain range, and the important mining resources in place in that area, transformed Cástulo into the largest city in the Iberian Oretania [26, 27]. Cástulo maintained contacts and relationships with many different and foreign populations; Phoenicians, Tartessians, Carthaginians and Greeks were among the merchants that helped enrich Cástulo both economically and culturally [27]. Cástulo's importance in the Roman Empire is vastly recognized due to its role in the Second Punic War (218–201 B.C.) [26, 27].

Dated at the end of the first century AD, the *Mosaico de los Amores* (Fig. 1) was found within a large building (33 × 12 m), oriented approximately north–south, during the archaeological excavations carried out in 2011–2013. The dating and importance of the building seem to indicate that its construction was dedicated to the imperial cult in honour of Emperor Domitian [28–30]. This well-preserved mosaic (11,75 m × 6 m) displays two main central themes, the Judgement of Paris and the myth of Selene and Endymion, surrounded by rhombus with animal depictions (wild boar, lion, horse, tiger, deer and lioness), as well as geometrical patterns and with a border of six half-circles depicting hunting scenes with Eroti or *Amores* (Fig. 1) [28]. Allegorical representations of the four seasons adorn the four corners of the mosaic (Fig. 1). These anthropomorphic representations of spring, summer, autumn and winter follow the exquisite design, iconography and quality of the seasons found in the Roman city of Itálica (Santiponce, Seville) [28]. This study will only focus on the stone and glass tesserae that constitute the representations of spring and summer (Fig. 2).

Prior to any measurement, each tessera was cleaned with a plastic brush and wiped with a sponge drenched in ethanol to diminish surface contamination.

Fig. 1 The Mosaico de los Amores (Linares, Spain), displaying the Judgement of Paris and the myth of Selene and Endymion, surrounded by rhombus with animal depictions, a border of six half-circles depicting hunting scenes with Eroti or Amores, and allegorical representations of the four seasons in the four corners of the mosaic. The anthropomorphic representation of spring can be found in the top right corner, while the depiction of summer can be seen on the top left corner

Fig. 2 Anthropomorphic representations of spring (left) and summer (right) from the Mosaico de los Amores (Linares, Spain)

2.2 Certified reference material

Two reference materials were analysed—Standard Reference Material® 610 and Standard Reference Material® 611—certified by the National Institute of Standards and Technology (NIST; Department of Commerce, United States of America). These two reference materials have the same certified mass fraction values. The recommended concentrations reported by Pearce et al. 1997 were used in this study [31].

Fig. 3 In situ measurements using **a** both instruments (Bruker™ Tracer III SD® hXRF in white) and **b** the Olympus™ Innov-X Delta Premium hXRF with the soil foot (U8990900) accessory

2.3 Methods

2.3.1 Bruker™ Tracer III SD®

The Bruker™ Tracer III SD® handheld XRF is equipped with a silicon drift 10 mm^2 XFlash ® detector (SDD) with an energy resolution of 149.68 eV for Mn Kα radiation at a count rate of 100 kcps, and a Rh target delivering a polychromatic X-ray beam of 3×3 mm^2. Despite the fact that this equipment can be fully battery-operated, the presence of an on-site portable generator allowed the instrument to be controlled using a portable computer (Fig. 3a) and the S1 PXRF software (Bruker™). Spectra were acquired under the following operating conditions: 40 kV, 11 μA and real time of 60 s. Given its size, each tessera was analysed only once. The visualization and the accurate positioning of the measurement spot was provided by the integrated camera of the instrument. The certified reference material NIST SRM 610 was measured using the same current and voltage but under a live time of 120 s. The ARTAX (Bruker™) software was used for spectral evaluation (postprocessing). Net counts of the elements were normalized to the Kα line of Rh [8, 16, 32]. The ANDAD software was used to perform PCA analysis of the normalized net counts [33].

2.3.2 Olympus™ Innov-X Delta premium

The Olympus™ Innov-X Delta Premium is a battery-operated handheld XRF instrument (Fig. 3b). It is equipped with a large-area (20 mm^2) silicon drift detector (SDD) and a Rh anode X-ray tube delivering a 3×3 mm^2 collimated X-ray beam (5×5 mm^2 when uncollimated). A two-beam mode (Geochem Mode) was used to analyse the selected tesserae. This mode allows spectra to be recorded sequentially using two different conditions: (a) 10 kV, 200 μA and no filter; (b) 40 kV and 100 μA with an aluminium filter. The spectra generated by each beam were recorded during a real time of 300 s. This equipment also has a camera that allowed the correct positioning of the instrument and the visualization of the analysed area. Each sample was analysed in one location. The certified reference material NIST SRM 611 was measured using the same current and voltage but under a live time of 120 s. The acquired spectra were processed using the ARTAX (Bruker™) software, and the generated net areas of the fluorescence lines were normalized to the counts of the Rh Kα lines [8, 16, 32] of the 40 kV mode, as these are not present in the 10 kV mode. The ANDAD software was used to perform PCA analysis of the normalized net counts [33].

Table 1 Overview of the main characteristics, as reported by the manufacturers, of the handheld XRF instruments used in this study

	Tracer III SD®	Innov-X Delta Premium
Manufacturer	Bruker™	Olympus™
Weight (kg)	2.04 kg with battery and PDA 1.63 kg without battery and PDA	1.74 kg with battery (with integrated touch screen) 1.52 kg without battery (with integrated touch screen)
Size (cm) (L × W × H)	30 × 10 × 28	26 × 9 × 24
Detector	Silicon drift 10 mm^2 XFlash® Detector	Large-area silicon drift detector
Vacuum pump	Offered as an accessory (not used in this study)	Not offered as an accessory
Power source	Removable Li-ion batteries or AC adapter	Removable Li-ion batteries or AC power unit
Operation	Laptop or iPAQ PDA	Laptop or integrated touch screen

3 Characteristics and on-field applicability

The main characteristics of the two handheld XRF instruments used in the study of the *Mosaico de los Amores* are presented in Table 1.

Mosaics are composed of small fragments of different and often heterogeneous materials known as tesserae. The tesserae, arranged in order to create artistic representations of figures, motifs and patterns, are generally made of ceramic, tile, stone or glass.

X-ray fluorescence has been widely used in the study of mosaics (e.g. [6, 7, 9–12, 15]). When tackling a large number of samples, hXRF, in particular, has been found to be rather useful in order to group materials [9, 10, 15] and to establish affinities between chemical elements [11]. However, one of the largest limitations posed by the use of hXRF is the detection of low-Z elements, due to the strong absorption of low-energy X-rays by air and by the Be window of the detector. The inability of hXRF instruments to generate high vacuum hinders their capability to correctly detect and quantify these elements [22]. The determination of Na, for instance, an element commonly present in glass, ceramics and stones, is generally not feasible even when present in relatively high concentrations (ca. 3.5 wt%) [22]. However, the use of a helium attachment capable of producing a helium flush or purge can circumvent this problem, enabling the detection of low-Z elements down to sodium [34].

Many hXRF users opt for employing a two-step methodology with different measurement conditions for light and heavy element analysis (e.g. [9–11, 13]). The two-beam mode present in the Olympus™ Innov-X Delta Premium instrument mimics this two-step process, freeing the user from having to manually change the conditions after every analysis or from remeasuring all samples at a later date using a second set of conditions as is necessary when using the Bruker™ Tracer III SD® instrument.

In order to evaluate the capabilities of each hXRF instrument in the detection of low-, mid- and high-Z elements, certified reference materials were analysed using the conditions described in the methodology section. Detection limits for each element are calculated using Eq. (1):

$$\mathrm{DL} = \frac{3 \times \sqrt{I_\mathrm{p}}}{I_\mathrm{b}} \times c \tag{1}$$

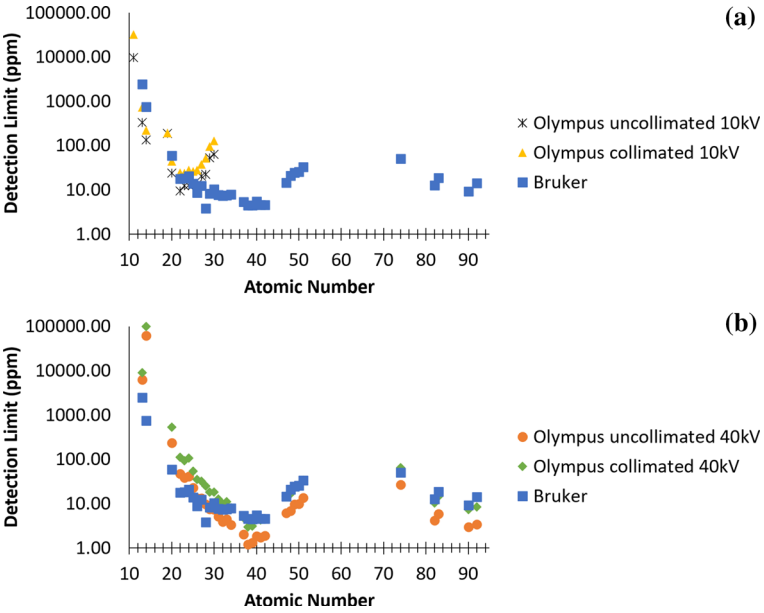

Fig. 4 Graphic representation of the detection limits calculated for each chemical element measured using the Bruker™ Tracer III SD® hXRF and the Olympus™ Innov-X Delta Premium instrument

where I_p corresponds to the net peak intensity of an element, I_b to the background intensity (i.e. the area of the background below the peak), and c is the concentration of the element in the certified reference material. The calculated detection limits of the Bruker™ Tracer III SD® hXRF and the Olympus™ Innov-X Delta Premium instrument can be found in Online Resource 1 and Fig. 4.

As seen in Fig. 4, the detection limits for the Olympus™ Innov-X Delta Premium instrument were calculated for measurements performed using a collimated (3×3 mm^2) and an uncollimated (5×5 mm^2) X-ray beam; the Bruker™ Tracer III SD® instrument, on the other hand, delivers a polychromatic X-ray beam of 3×3 mm^2. As expected, measurements performed using an uncollimated X-ray beam have lower detection limits, which can be explained by the larger volume of material analysed and the higher photon flux from the instrument impinging this volume. However, while the Olympus™ Innov-X Delta Premium hXRF, using measurement conditions for light elements (10 kV, 200 μA), has lower detection limits than the Bruker™ Tracer III SD® instrument operating under conditions that are not recommended for light element detection (40 kV, 11 μA) for $Z < 20$, the same cannot be said for heavier elements (Fig. 4a). When comparing both instruments operating at the same voltage (40 kV) and using a 3×3 mm^2 polychromatic X-ray beam, it becomes clear that the Bruker™ Tracer III SD® hXRF has lower detection limits than the Olympus™ Innov-X Delta Premium instrument at $20 \leq Z < 27$, while both instruments have similar detection limits for elements with $Z \geq 31$ (Fig. 4b).

As seen in Table 1, the size and weight of both instruments used in this study are very similar, as is the power source, making both instruments easily transportable and operated in challenging in situ conditions. As both instruments also possess integrated cameras, the accurate positioning of the instruments is straightforward. However, while the Bruker™ Tracer III SD® handheld XRF needs to be manually held in place to ensure its steadiness

throughout data acquisition, the soil foot (U8990900) accessory of the Olympus™ Innov-X Delta Premium instrument keeps the analyser level on the ground hands-free, when measuring horizontally oriented subjects. The lower detection limits of the Olympus™ Innov-X Delta Premium hXRF for light elements when operating under the manufacturer's recommended settings are also noteworthy.

4 Comparative analysis of tesserae from the anthropomorphic representations of spring and summer (*Mosaico de los Amores*)

Forty-one tesserae from the anthropomorphic representation of spring and 16 tesserae from the depiction of summer (*Mosaico de los Amores*, Linares, Spain) were analysed using two handheld XRF instruments—the Bruker™ Tracer III SD® and the Olympus™ Innov-X Delta Premium. All spectra collected were processed using the Artax (Bruker™) software in order to obtain semi-quantitative data. The generated net areas of the fluorescence lines were normalized to the counts of the Rh Kα lines [8, 16, 32] in order to compensate for differences in morphology, which influence the distance between the instrument and the sample and, therefore, the total irradiated mass per sample. The disparity between the numbers of analysed tesserae from each depiction can be explained by the chromatic richness of the spring scene.

A comparison between the raw spectra acquired using the Bruker™ Tracer III SD® and the Olympus™ Innov-X Delta Premium hXRF (Fig. 5) emphasizes the differences between these two instruments. The two-beam mode of the Olympus™ hXRF permitted the automatic acquisition of two spectra hereafter designated by Olympus A (0–40 keV) and Olympus B (0–10 keV). As seen in Fig. 5a, the low-Z elements are poorly identifiable in the Olympus A spectra, while elements with $Z \geq 13$ are clearly visible in the Bruker spectra. However, low-Z elements which are generally difficult to detect using hXRF devices, such as Na ($Z = 11$), can be identified in the Olympus B spectra (Fig. 5b). This is consistent with the previously discussed detection limits (Fig. 4 and Online Resource 1). The detection of sodium is particularly important in archaeometric studies which include man-made glass. While silicate man-made glass is the most common type of glass found in archaeological contexts, three main types of fluxing agents have been used throughout time—natron, soda plant ash and potash plant ash—to lower the melting temperature of sand. Natron, the common name given to evaporitic deposits rich in sodium carbonate and sodium bicarbonate, was used to manufacture man-made glass artefacts in Europe and the Levantine region from the beginning of the first millennium B.C. until the ninth century A.D. [35]. Natron was then replaced by the sodium-rich ash of halophytic plants in the Islamic Near East, and by potassium-rich wood ash in Western Europe [35]. As most man-made glass classifications rely on the correct identification of the fluxing agent used (e.g. [36]), employing analytical techniques capable of correctly assessing the Na content has proven to be extremely important [8, 16, 37]. It is important to note, however, that, under burial conditions, glass can suffer alteration processes which have a significant impact on its chemical composition; alkali elements, such as sodium and potassium, are particularly affected by selective leaching, while a combination of selective leaching and glass dissolution can lead to the precipitation of hydrous silica-gel layers as newly formed alteration products [37, 38].

Elemental bi-plots using the normalized net counts of the Kα or Lα lines of the detected elements were used as a first approach to better visualize differences between the tesserae analysed. This approach also highlights the difference between the Bruker™ Tracer III SD® and the Olympus™ Innov-X Delta Premium XRF instruments, and the influence of the two-beam mode of the latter. Despite the fact that the normalized net counts of the Kα lines

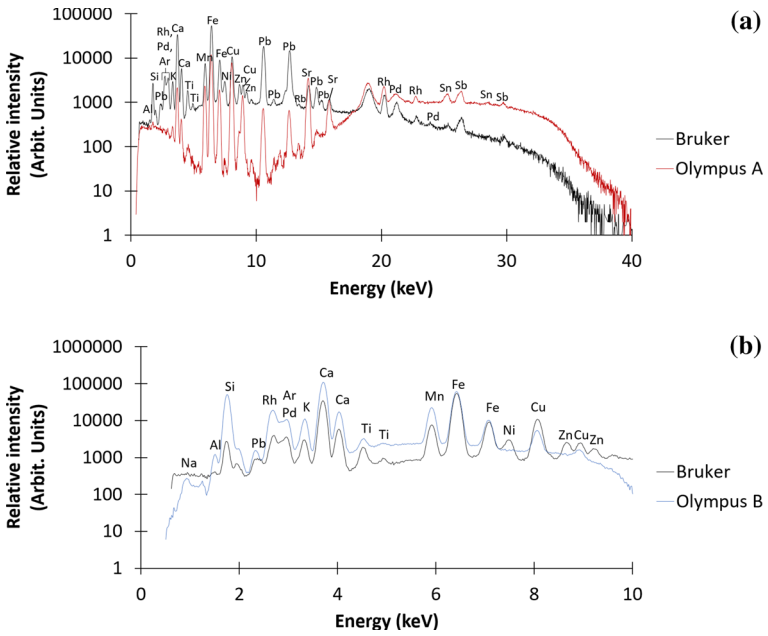

Fig. 5 Comparison between the raw spectra acquired using the Bruker™ Tracer III SD® and the Olympus™ Innov-X Delta Premium hXRF instruments. The influence of the two-beam mode of the Olympus™ instrument should be noted. **a** Spectrum of sample 8 acquired using the Bruker ™ instrument and the 0–40 keV beam of the Olympus™ hXRF; b) spectrum of sample 8 acquired using the Bruker ™ instrument and the 0–10 keV beam of the Olympus™ hXRF

of low-Z elements are ca. 3–10 times higher when using the Olympus™ instrument, the results obtained using both instruments are similar (e.g. Figures 6 and 7). As seen in Figs. 6 and 7, three groups of tesserae can easily be distinguished using both instruments; the first group (Group I) enriched in calcium most likely corresponds to limestone tesserae, while the second group (Group II) enriched in Si corresponds to glass tesserae. The black tesserae that make up Group III are enriched in Si, Al, K, Fe, Ti and Rb (Fig. 8) which suggests that they was made from a rock with high amounts of aluminosilicates and Fe–Ti oxides, possibly an igneous or metamorphic rock, or a sedimentary rock deriving from the former. A list of samples subdivided into these groups can be found in Table 2.

These three compositional groups are also visible when principal component analysis (PCA) was performed using the normalized net counts of each element (Fig. 9). However, as seen in Fig. 9, the PC1-PC2 score plot of the Olympus dataset yielded clearer sample grouping, as each group was confined to a quadrant—Group I with negative PC1 values but positive PC2 values, Group II with positive PC1 values but negative PC2 values and Group 3 with positive PC1 and PC2 values—whereas in the case of the Bruker dataset, samples Sp14 and Sp32 (limestone tesserae) could be mistakenly included in Group II.

The Iberian-Roman city of Cástulo is located in a geologically diverse region which comprises a wide assortment of sedimentary rocks, such as conglomerates, sandstones, limestones and dolomites, as well as granitic outcrops [39]. The stone tesserae, including those that constitute groups I and III, could, therefore, have been manufactured on-site, using local materials. However, given the ubiquitous nature of these raw materials, they could also have been manufactured elsewhere.

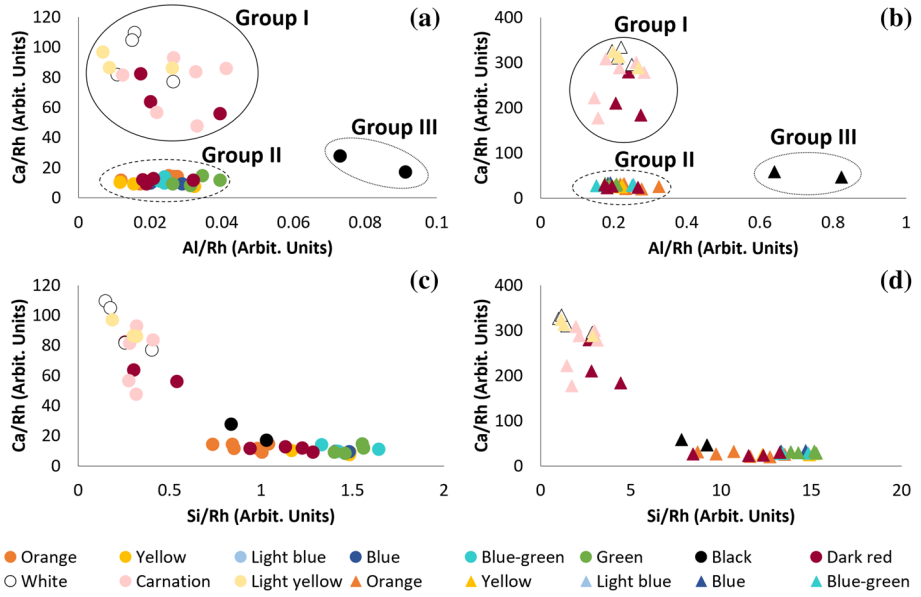

Fig. 6 Elemental bi-plots using the normalized net counts of the Kα lines of Ca and Al (**a** and **b**) and Ca and Si (**c** and **d**) from the spring scene. Results obtained using the Bruker™ Tracer III SD® hXRF are represented by circles, while triangles are used to indicate data acquired using the Olympus™ Innov-X Delta Premium instrument. Groups I, II and III are described in the text

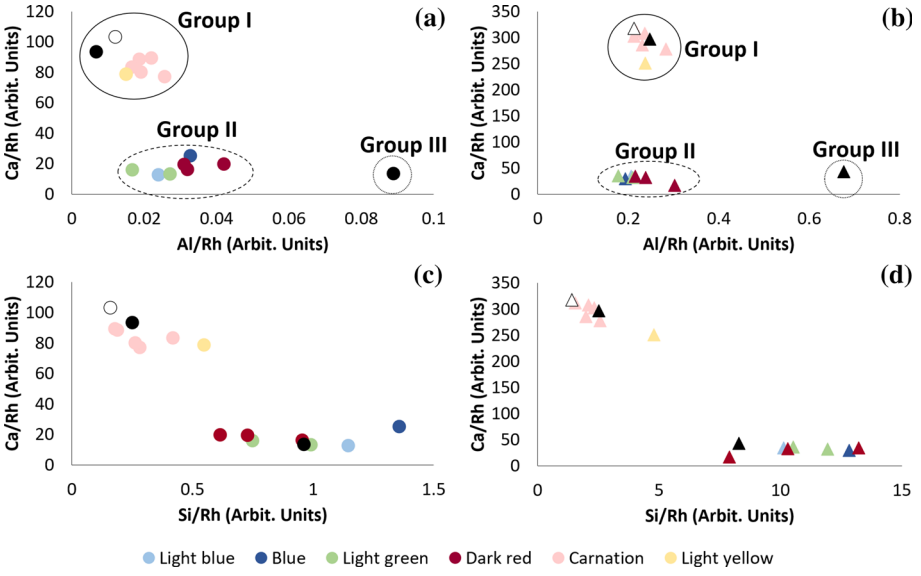

Fig. 7 Elemental bi-plots using the normalized net counts of the Kα lines of Ca and Al (**a** and **b**) and Ca and Si (**c** and **d**) from the summer scene. Results obtained using the Bruker™ Tracer III SD® hXRF are represented by circles, while triangles are used to indicate data acquired using the Olympus™ Innov-X Delta Premium instrument. Groups I, II and III are described in the text

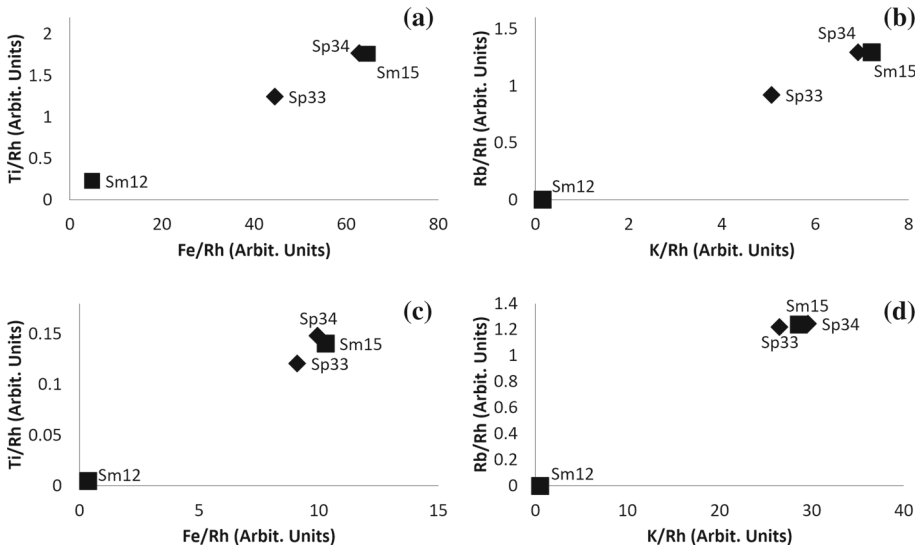

Fig. 8 Elemental bi-plots using the normalized net counts of the Kα lines of Ti, Fe, Rb and K of the black coloured tesserae. Results obtained using the Bruker™ Tracer III SD® hXRF (**a** and **b**) and the Olympus™ Innov-X Delta Premium instrument (**c** and **d**). Data points from the spring scene are represented by rhombus, while squares are used to indicate measurement points from the summer depiction

Table 2 Subdivision of the tesserae based on their overall composition

	Spring scene	Summer scene
Group I (limestone)	Sp10, Sp14, Sp15, Sp23, Sp24, Sp25, Sp26, Sp27, Sp28, Sp29, Sp30, Sp31, Sp32, Sp35, Sp36 and Sp42	Sm4, Sm5, Sm6, Sm11, Sm12 Sm13, Sm14 and Sm19
Group II (glass)	Sp1, Sp2, Sp3, Sp4, Sp5, Sp6, Sp7, Sp8, Sp9, Sp11, Sp12, Sp13, Sp17, Sp18, Sp19, Sp20, Sp21, Sp22, Sp37, Sp38, Sp39, Sp40 and Sp41	Sm1, Sm2, Sm8, Sm9, Sm10, Sm16 and Sm18
Group III (aluminosilicate-rich rock)	Sp33 and Sp34	Sm15

Tesserae marked as Sp and Sm are from the spring and summer scenes, respectively

The colour of limestones is generally attributed to the presence of impurities (i.e. noncarbonate minerals or organic materials), but is also related to the redox conditions present in the environment at the time of the rock's formation [40, 41]. Relatively pure carbonates have colours ranging from white to light yellow and light grey; organic-rich limestones present dark grey or black hues, while iron-rich minerals are responsible for pinkish to reddish colours [41, 42]. The presence of iron and/or organic matter can explain the wide variety of hues of the limestones used to produce the white, light yellow, carnation, dark red and black coloured tesserae from Group I (Online Resource 2).

Given their colour and overall composition, the samples of Group II were found to be glass tesserae (Online Resource 3). The detection of Na using the Olympus™ Innov-X Delta

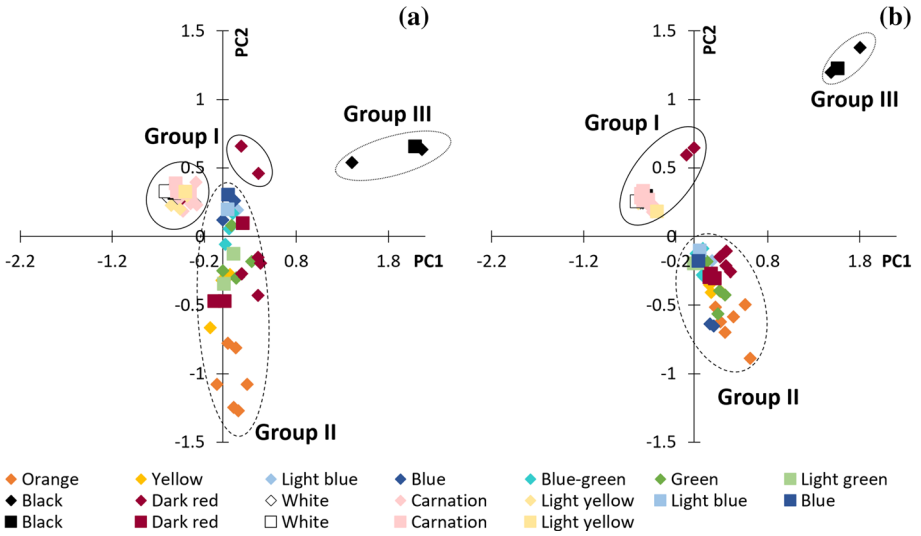

Fig. 9 Score plots for PC1 and PC2 of the datasets collected by both hXRF instruments: **a** the Bruker™ Tracer III SD® hXRF; and **b** the Olympus™ Innov-X Delta Premium hXRF. Data points from the spring scene are represented by rhombus, while squares are used to indicate measurement points from the summer depiction. Groups I, II and III are described in the text

Premium hXRF most likely indicates a natron-lime-silicate composition, as natron was the only fluxing agent used in Roman times [43].

Significant amounts of lead were also found in several glass tesserae. This element was found in conjunction with copper in the orange and green tesserae as well as in the blue-green tessera Sp41 and the dark red tesserae Sp3, Sp4, Sm8 and Sm9 (Figs. 10a and 11a). Copper, present as divalent ions, metallic Cu or cuprite (Cu_2O), is among the most common colouring agents used in glass production. Cu^{2+} ions impart a turquoise colour to glass [44], while metallic Cu and cuprite crystals are used to manufacture orange, red and brown hues [45]. Silvestri et al. (2015) found that the amount of Cu and Pb can influence the type of Cu-rich phase present in glass, and ultimately the final orange to brown glass hue [45]. La Delfa et al. (2008), on the other hand, determined that green tesserae can be produced when combining divalent copper ions and lead, with the amount of lead greatly influencing the green hue obtained [46].

As seen in Figs. 10b and 11b, iron is present in varying amounts, in the glass tesserae displaying blue and green hues. Iron can be used to produce a wide range of hues from yellow to green depending on the Fe^{2+}/Fe^{3+} ratio [44]. As Fe^{2+} and Fe^{3+} impart a blue and pale-yellow tint to glass, respectively, the redox conditions used during the manufacturing process are determinant to the final hue obtained [44]. Moreover, iron is a common impurity in many of the raw materials used in glass production, with most glass containing ca. 0.3 wt% of FeO [44]. In fact, iron seems to have been used as the colouring agent to produce the light green tesserae (Figs. 10b and 11b).

Copper divalent ions were used to produce the blue-green tesserae and the light blue tessera Sp38, while cobalt ions were generally used to produce darker blue hues (Figs. 10c and 11c). Cobalt divalent ions, when in tetrahedral coordination, impart a deep blue purplish hue to glass [45]. As previously mentioned, the presence of iron (Figs. 10b and 11b) most likely influenced the final hue of these glass tesserae.

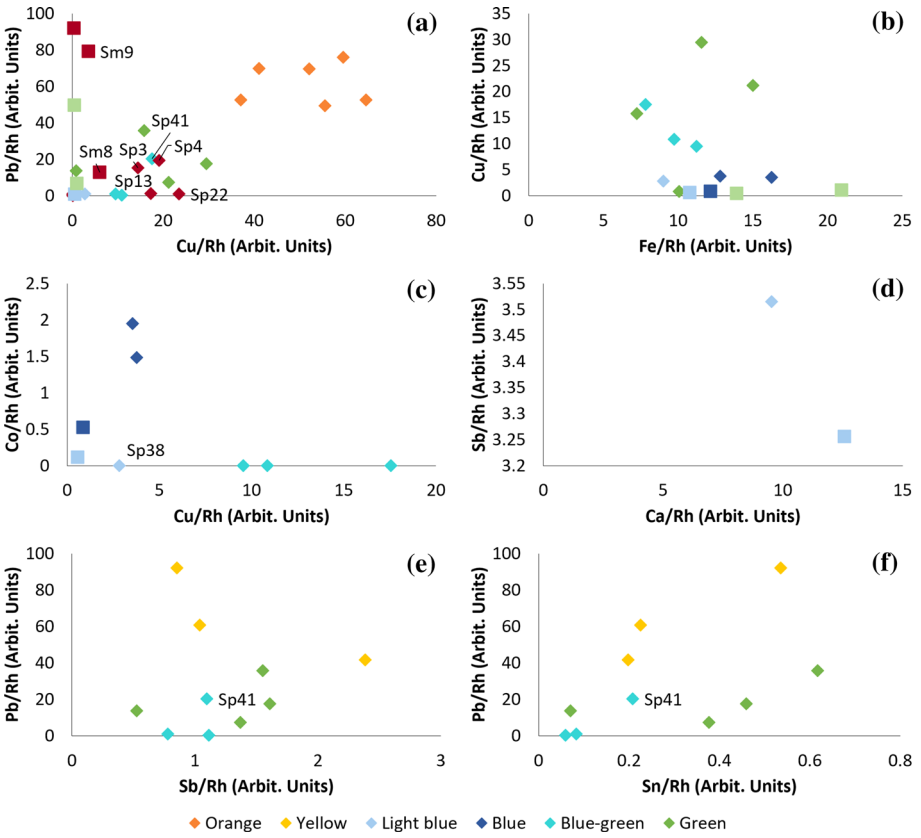

Fig. 10 Elemental bi-plots of **a** Pb/Rh-Cu/Rh; **b** Cu/Rh-Fe/Rh; **c** Co/Rh-Cu/Rh; **d** Sb/Rh-Ca/Rh; **e** Pb/Rh-Sb/Rh; **f** Pb/Rh-Sn/Rh. Data obtained using the Bruker™ Tracer III SD® hXRF. Measurement points from the spring scene are represented by rhombus, while squares are used to indicate samples from the summer depiction

Calcium antimonates were also most likely used as opacifying agents in the light blue tesserae (Figs. 10d and 11d). In fact, calcium antimonate ($CaSb_2O_6$) was identified in the baby blue tesserae of one of the Eros scenes by in situ micro-Raman spectroscopy [47]. Calcium antimonates have been used in glass production since the thirteenth century B.C. to obtain opaque light blue and white coloured glass [43, 48].

Both lead and antimony were found to be present in the yellow tesserae (Figs. 10e and 11e). This is consistent with the use of lead antimonate, a yellow-coloured opacifier used throughout the Roman period [49]. Lead antimonates, also referred to as bindheimite ($Pb_2Sb_2O_6(O,OH)$) given their equivalent crystalline structure, were used to produce opaque yellow and green glass [49]. As seen in Figs. 10e and 11e, this compound was also used in the production of the green tesserae and the blue-green tessera Sp41, contributing to the hue displayed by these glass objects.

Studies have shown that the crystalline structure of bindheimite can accommodate small amounts of elements such as tin [49]. Given the relationship between lead, tin and antimony (Figs. 10f and 11f), these lead antimonate compounds known as a ternary Pb–Sb–Sn oxides

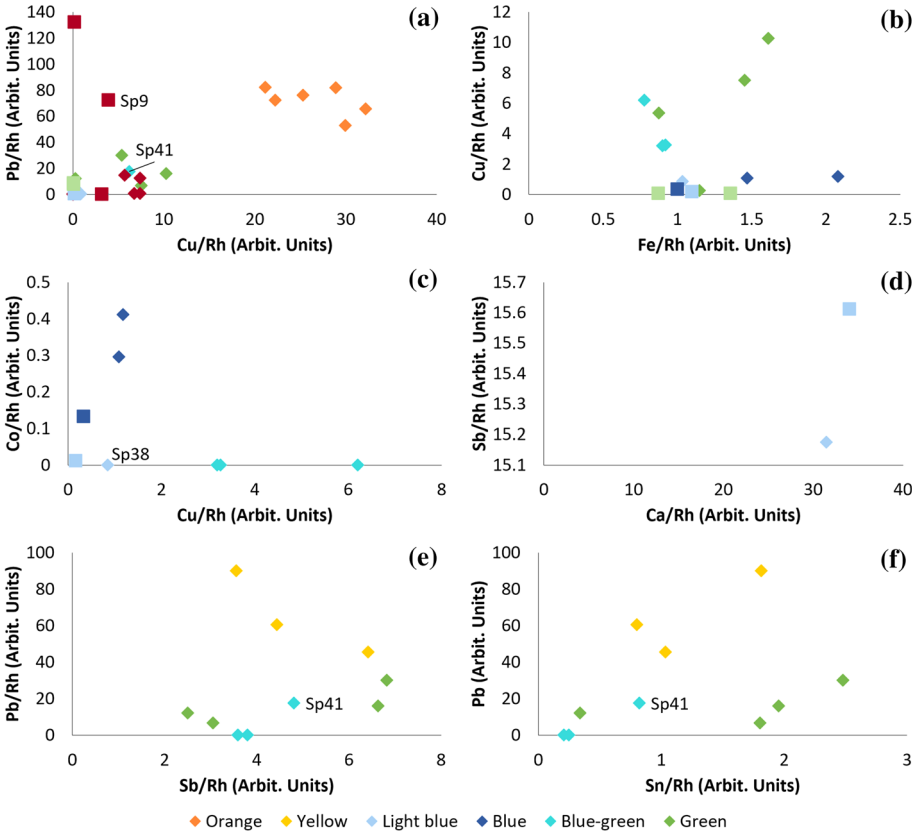

Fig. 11 Elemental bi-plots of **a** Pb/Rh–Cu/Rh; **b** Cu/Rh–Fe/Rh; **c** Co/Rh–Cu/Rh; **d** Sb/Rh–Ca/Rh; **e** Pb/Rh–Sb/Rh; **f** Pb/Rh–Sn/Rh. Data obtained using the Olympus™ Innov-X Delta Premium hXRF. Measurement points from the spring scene are represented by rhombus, while squares are used to indicate samples from the summer depiction

[16] seem to have been used to produce the yellow and green tesserae and the blue-green tessera Sp41 found in the spring scene.

5 Final remarks

In this study, the Bruker™ Tracer III SD® and the Olympus™ Innov-X Delta Premium were compared and evaluated using tesserae from *Mosaico de los Amores* (Linares, Spain). An overview of the applicability and the performance of the two handheld XRF instruments is presented in Table 3.

Given their portability, the user-friendly nature of their operating systems and their overall performance, both the Bruker™ Tracer III SD® and the Olympus™ Innov-X Delta Premium are highly recommended for in situ campaigns in Cultural Heritage studies. However, the Olympus™ Innov-X Delta Premium hXRF has two features that can be crucial in the study of unmovable artworks: a) the two-beam mode which allows two sequential measurements, using conditions optimized for light and heavy element analysis, to be performed in the same

Table 3 Overview of the applicability and performance of the hXRF instruments using the reported analytical conditions (min. +, max. +++)

	Bruker™ Tracer III SD®	Olympus™ Innov-X Delta Premium
Portability and ease of use	+++	+++
Detection of low-Z elements	++	+++
Overall performance	+++	+++

location; and b) the soil foot (U8990900) accessory which unburdens the user for having to manually hold the instrument in place when measuring horizontally oriented subjects.

The detection limits calculated for each element also point towards a better detection of low-Z elements when using the two-beam mode of the Olympus™ Innov-X Delta Premium hXRF. However, it should be noted that the Bruker™ Tracer III SD® instrument was not operated under the manufacturer's recommended settings for low-Z element detection and quantification. This study underlines the importance of systems that allow the analysis of the same point with analytical conditions optimized for different chemical elements.

Acknowledgements The authors would like to recognize the support of the project Cástulo, Investigación arqueométrica y transferencia social (HAR2016-74917-R) and the Archaeological Area of Cástulo (Linares, Spain). The financial support of the project UID/Multi/04449/2017 (POCI-01-0145-FEDER-007649) funded by Fundação para a Ciência e Tecnologia and the European Regional Development Fund is also acknowledged. Mafalda Costa would like to acknowledge FCT for her Ph.D. Fellowship (SFRH/BD/128889/2017). Anastasia Rousaki greatly acknowledges the Research Foundation–Flanders (FWOVlaanderen) for the postdoctoral fellowship (number: 12X1919N) and for the travel grant for a short stay abroad (number: K207718N). Pieter Tack also greatly acknowledges the Research Foundation-Flanders (FWOVlaanderen) for the postdoctoral fellowship (number: 12Q7718N).

Data Availability Statement This manuscript has data included as electronic supplementary material.

Funding This study was funded by the project Cástulo, Investigación arqueométrica y transferencia social (HAR2016-74917-R) and by the project UID/Multi/04449/2017 (POCI-01-0145-FEDER-007649).

Compliance with ethical standards

Conflicts of interest The authors declare that they have no conflicts of interest.

Code availability Not applicable

References

1. E. Frahm, R.C.P. Doonan, J. Archaeol. Sci. **40**, 1425–1434 (2013)
2. L. De Viguerie, A. Duran, A. Bouquillon, V.A. Solé, J. Castaing, P. Walter, Anal. Bioanal. Chem. **395**, 2219–2225 (2009)
3. T. Pantazis, J. Pantazis, A. Huber, R. Redus, X-Ray Spectrom. **39**, 90–97 (2010)
4. S.C. Phillips, R.J. Speakman, J. Archaeol. Sci. **36**, 1256–1263 (2009)
5. N.W. Brand, C.J. Brand, Geochem. Explor. Environ. Anal. **14**, 125–138 (2014)
6. P. Croveri, I. Fragalà, E. Ciliberto, Appl. Phys. A Mater. Sci. Process. **100**, 927–935 (2010)
7. M.S. Gill, T. Rehren, Archaeometry **53**, 22–36 (2011)
8. B. Dal Bianco, U. Russo, J. Non. Cryst. Solids **358**, 368–378 (2012)

9. P. Avino, P. Moioli, A. Rosada, C. Seccaroni, Herit. Sci. **1**, 1–8 (2013)
10. F. Licenziati, T. Calligaro, J. Archaeol. Sci. Rep. **7**, 640–648 (2016)
11. A. Moropoulou, N. Zacharias, E.T. Delegou, B. Maróti, Z.S. Kasztovszky, Microchem. J. **125**, 170–184 (2016)
12. T. Pereira, C. Andrade, M. Costa, A. Farias, J. Mirão, A.F. Carvalho, Quat. Int. **412**, 135–144 (2016)
13. L. Rosado, J. Van Pevenage, P. Vandenabeele, A. Candeias, M. da Conceição Lopes, D. Tavares, R. Alfenim, N. Schiavon, J. Mirão, Measurement **118**, 262–274 (2018)
14. I. Marcaida, M. Maguregui, H. Morillas, N. Prieto-Taboada, M. Veneranda, S. Fdez-Ortiz de Vallejuelo, A. Martellone, B. De Nigris, M. Osanna, J.M. Madariaga, Herit. Sci. **7**, 3 (2019)
15. M. Costa, A.M. Arruda, R. Barbosa, P. Barrulas, P. Vandenabeele, J. Mirão, Microsci. Microanal. **25**, 214–220 (2019)
16. M. Costa, P. Barrulas, L. Dias, M. da Conceição Lopes, J. Barreira, B. Clist, K. Karklins, M. da Piedade de Jesus, S. da Silva Domingos, P. Vandenabeele, J. Mirão, Microchem. J. **149**, 103990 (2019)
17. I. Liritzis, N. Zacharias, in *X-Ray Fluorescence Spectrometry (XRF) in Geoarchaeology*, ed. by M.S. Shackley (Springer, New York, 2011), pp. 109–144
18. P.J. Potts, F. Bernardini, M.C. Jones, O. Williams-Thorpe, P.C. Webb, X-Ray Spectrom. **35**, 8–18 (2006)
19. M.S. Shackley, in *X-Ray Fluorescence Spectrometry (XRF) in Geoarchaeology*, ed. by M.S. Shackley (Springer, New York, 2011), pp. 7–44
20. M. Rouillon, M.P. Taylor, Environ. Pollut. **214**, 255–264 (2016)
21. D.J. Kalnicky, R. Singhvi, J. Hazard. Mater. **83**, 93–122 (2001)
22. A.M.W. Hunt, R.J. Speakman, J. Archaeol. Sci. **53**, 626–638 (2015)
23. D. Sokaras, A.G. Karydas, A. Oikonomou, N. Zacharias, K. Beltsios, V. Kantarelou, Anal. Bioanal. Chem. **395**, 2199–2209 (2009)
24. G.T. Jones, L.M. Fontes, R.A. Horowitz, C. Beck, D.G. Bailey, Am. Antiq. **77**, 351–367 (2012)
25. N. Goodale, D.G. Bailey, G.T. Jones, C. Prescott, E. Scholz, N. Stagliano, C. Lewis, J. Archaeol. Sci. **39**, 875–883 (2012)
26. C. Choclán Sabina, in V. Leis Sánchez, L. Martínez Aguilar, L. Rabaneda Sánchez (eds.) *Actas I Congreso de Historia de Linares, coord*. (Centro de Estudios Linarenses: Diputación Provincial de Jaén, Jaén, 2012), pp. 29–47
27. J.M. Blázquez, M.P. García-Gelabert, Estudios de arqueología ibérica y romana. Homenaje a Enrique Pla Ballester, Trabajos Varios del Servicio de Investigación Prehistórica **89**, 391–396 (1992)
28. G. Lopéz Monteagudo, Siete Esquin. **6**, 117–125 (2014)
29. C. Pérez Bareas, Depósitos arqueológicos, sucesión estratigráfica y fases de ocupación. Siete Esquin. **6**, 61–72 (2014)
30. T. López Martínez, @rqueología y Territ. **12**, 165–175 (2015)
31. N.J.G. Pearce, W.T. Perkins, J.A. Westgate, M.P. Gorton, S.E. Jackson, C.R. Neal, S.P. Chenery, Geostand. Newsl. J. Geostand. Geoanal. **21**, 115–144 (1997)
32. D. Lauwers, A. Candeias, A. Coccato, J. Mirao, L. Moens, P. Vandenabeele, Spectrochim. Acta Part A Mol. Biomol. Spectrosc. **157**, 146–152 (2016)
33. A. J. Gonçalves de Sousa, Programa ANDAD. (2007) http://biomonitor.ist.utl.pt/~ajsousa/Andad.html. Accessed 26 June 2019
34. S. Röhrs, H. Stege, X-Ray Spectrom. **33**, 396–401 (2004)
35. A. Shortland, L. Schachner, I. Freestone, M. Tite, J. Archaeol. Sci. **33**, 521–530 (2006)
36. B. Gratuze, K. Janssens, in *Comprehensive Analytical Chemistry 42*, ed. by K. Janssens, R. Van Grieken (Elsevier, Amesterdam, 2004), pp. 663–712
37. M. Costa, A.M. Arruda, L. Dias, R. Barbosa, J. Mirão, P. Vandenabeele, J. Raman Spectrosc. **50**, 250–261 (2019)
38. A. Silvestri, G. Molin, G. Salviulo, J. Non-Cryst. Solids **351**, 1338–1349 (2005)
39. L.M. Martín Parra, J. Matas, F.J. Roldán, A. Martín-Serrano, D. Martínez Poyatos, F. González Lodeiro, Mapa Geológico de España, Escala 1:200.000, Hoja 70 (Linares) (Instituto Geológico y Minero de España, Madrid, 2009)
40. R.C. Freas, J.S. Hayden, C.A. Pryor Jr., in *Industrial Minerals & Rocks: Commodities, Markets and Uses*, ed. by J.E. Kogel, N.C. Trivedi, J.M. Barker, S.T. Krukowski (Society for Mining, Metallurgy, and Exploration, Inc, Littleton, 2009), pp. 581–597
41. Y. Cai, X. Hu, X. Li, Y. Pan, Cretac. Res. **38**, 97–102 (2012)
42. D.A.V. Stow, *Sedimentary Rocks in the Field: A Colour Guide*, 5th edn. (Manson Publishing Ltd, London, 2010), p. 320
43. C. Moretti, S. Hreglich, in *Modern Methods for Analysing Archaeological and Historical Glass*, vol. I, ed. by K. Janssens (Wiley Ltd, Chichester, 2013), pp. 23–47
44. D. Möncke, M. Papageorgiou, A. Winterstein-Beckmann, N. Zacharias, J. Archaeol. Sci. **46**, 23–36 (2014)

45. A. Silvestri, S. Tonietto, G. Molin, P. Guerriero, Eur. J. Mineral. **27**, 225–245 (2015)
46. S. La Delfa, E. Ciliberto, L. Pirri, J. Cult. Herit. **9**, e117–e122 (2008)
47. A. Rousaki, M. Costa, D. Saelens, S. Lycke, A. Sánchez, J. Tuñón, B. Ceprián, P. Amate, M. Montejo, J. Mirão, P. Vandenabeele, J. Raman Spectrosc. (2019). https://doi.org/10.1002/jrs.5624
48. A.J. Shortland, Archaeometry **44**, 517–530 (2002)
49. S. Lahlil, M. Cotte, I. Biron, J. Szlachetko, N. Menguye, J. Susinib, J. Anal. At. Spectrom. **26**, 1040–1050 (2011)